

Terminal Wind Hazard Analyses Based on Assimilated Weather Data and Lagrangian Coherent Structures

BRENT KNUTSON,^{a,c} WENBO TANG,^a AND PAK WAI CHAN^b

^a*School of Mathematical and Statistics Sciences, Arizona State University, Tempe, Arizona*

^b*Hong Kong Observatory, Hong Kong, China*

(Manuscript received 1 February 2020, in final form 18 September 2020)

ABSTRACT: The operational light detection and ranging (lidar) data from the Hong Kong International Airport (HKIA) in China are assimilated in the six-nest, high-resolution Weather Research and Forecasting (WRF) Model. The existing radar data assimilation schemes in the WRF data assimilation (WRFDA) package have been adapted to accommodate the high temporal frequency and spatial resolution of the lidar observations. The weather data are then used to produce Lagrangian coherent structures to detect atmospheric hazards for flights. The coherent structures obtained from the various datasets are contrasted against flight data measured on aircraft. It is found that both WRF and WRFDA produce coherent structures that are more distinguishable than those obtained from two-dimensional retrieval, which may improve the detection of true wind shear hazards.

KEYWORDS: Lidars/Lidar observations; Differential equations; Pattern detection; Numerical weather prediction/forecasting; Transportation meteorology

1. Introduction

Low-level airflow disturbances near airports that are induced by weather, topography, and traffic may create hazardous conditions that adversely affect flight operations during takeoffs and landings. Accurate and fast detection of flow features that correspond to such disturbances present a challenge in aviation safety. In current airport operations, local weather forecasts as well as a network of in situ measurement data are incorporated to generate wind hazard alerts (Oude Nijhuis et al. 2018). At the Hong Kong International Airport (HKIA) in China, for example, a Terminal Doppler Weather Radar (TDWR), two light detection and ranging (lidar) systems, and a dense network of surface wind sensors monitor low-level wind changes at and near the airport in real time. All of these on-ground sensor data, along with forecasts based on broad prevailing meteorological conditions and aircraft reports via air traffic controller, are used to automatically generate “up to the minute” alerts for wind shear and/or turbulence. Operationally, the wind shear and turbulence warning system at Hong Kong Observatory issues microburst and wind shear alerts that are based on wind speed loss or gain and issues turbulence alerts that are based on the eddy dissipation rate within 3 n mi (1 n mi = 1.852 km) of the runway corridor. In the past few years, the rate of successful detection of wind shear events was about 90% (Hong Kong Observatory; https://www.hko.gov.hk/en/aviat/amt/windshear_warning.htm).

Pulsed Doppler lidars are suitable for detecting low-level wind shear in clear-air conditions, which accounts for nearly 90% of wind shear reports at HKIA (Shun and Lau 2002;

Shun and Chan 2008; Chan 2009; Chan and Lee 2012). Since their deployment in 2002 and 2006, a suite of studies has emerged based on lidar measurements. For example, Chan and Shao (2007) and Wong and Chan (2013) discussed using variational techniques to retrieve two-dimensional and three-dimensional velocity data from the line-of-sight (LOS) component measured by lidar; Chan et al. (2011), Chan (2012), and Lee and Chan (2014) discussed lidar-based velocity ramp, gradient, and F factor for wind shear alerts; and Chan (2010) and Hon and Chan (2014) discussed lidar-based eddy dissipation rate for turbulence alerts.

To complement the aforementioned studies that focus on metrics using Eulerian quantities, a Lagrangian framework has also been developed to detect hazardous airflow disturbances near the HKIA using lidar data. In this framework, flow features are extracted based on Lagrangian trajectories of air parcels, which highlight disturbances that persist over time and space and removes spurious transient data from Eulerian detection methods (Haller 2001). Accordingly, flow structures that are most dangerous to flight operations can be revealed.

In particular, using the 2D-var retrieval developed in Chan and Shao (2007), trajectories are integrated over a 5-min time window and, using the finite-domain-finite-time Lyapunov exponent (FDFTLE; Tang et al. 2010, 2011a) and meso-ellipticity (Hon et al. 2014), coherent structures are obtained to infer low-level flow structures near ground. These structures are compared to landing data from pilot reports. For example, in Tang et al. (2011b), 20 landing cases representing three different atmospheric conditions were analyzed. Based on a very restrictive metric of the Lagrangian coherent structures (LCS) to be within 150 m of the jolt measured on board as being relevant, a correlation of 60%–80% was found among the different scans. Following the FDFTLE framework, Kafiabad et al. (2013) analyzed 11 months of historical data. Using a conventional metric of 5-min detection range (Fawcett 2006), it is found that hazard detection based on the gradient of FDFTLE

^c Current affiliation: U.S. Bank, Charlotte, North Carolina.

Corresponding author: Wenbo Tang, wenbo.tang@asu.edu

alone generates a slightly inferior receiver operating characteristic when compared with the operational algorithm at HKIA, which is obtained from multiple sources of data. It is thus worthwhile to further explore the applicability of Lagrangian methods in airflow hazard detections.

To interpret the LCS obtained from only two-dimensional retrieval data in full three-dimensional flow fields, the FDFLE algorithm has also been applied to numerical weather prediction (NWP) models, and the results are compared with those based on 2D-var lidar retrievals and with pilot reports (Knutson et al. 2015). Using datasets from three independent NWP models, it is found that low-level Lagrangian flow structures are better revealed by only considering trajectories using two-dimensional velocity, as compared to using the full three-dimensional velocity data. This avoids inclusion of trajectory separation due to vertical shear near boundaries, which is more pronounced and do not necessarily lead to airflow hazards. It is also found that, among three NWP models studied [Weather Research and Forecasting (WRF) Model (Skamarock and Klemp 2008), Regional Atmospheric Modeling System (RAMS; Pielke et al. 1992), and the “FLOWSTAR” package (Carruthers et al. 1988)], the WRF Model, initiated from the NCEP Final Analysis (FNL) data, shows the closest resemblance to lidar-based flow structures using 2D-var and the pilot reports.

While lidar measurements are obtained in real time, the “ground truth” in 2D-var is only in the LOS velocity, and the velocity component orthogonal to the LOS is only constrained by smoothness and conservation of mass and momentum. Boundary conditions and topographic features are not factors in the cost function of the retrieval. On the other hand, WRF simulations in Knutson et al. (2015) were initiated using NCEP data, so assimilation of global in situ data is only present in the initial conditions and no incorporation of HKIA lidar measurements were considered. A natural step forward is to bridge the two efforts by incorporating lidar data in the WRF Model using its data assimilation capabilities (WRFDA). As such, the goal of this study is, to seek the feasibility of cycling high-resolution lidar data in WRFDA, for a continuous time window relevant to the small-scale Lagrangian analyses; and to generate and compare the LCS obtained from 2D-var, WRF, and WRFDA to the pilot reports taken as the “ground truth.”

Data assimilation techniques have been developed recently in NWP to meet the need of precision in operational forecasts and research purposes (Barker et al. 2004; Huang et al. 2009; Barker et al. 2012). Specifically, relevant to the NWP used in this study, radar data assimilation has been developed in WRF (Xiao et al. 2005; Wang et al. 2013; Choi et al. 2013; Sun and Wang 2013) and applied in forecasts (Xiao and Sun 2007; Routray et al. 2010). Radar observations share a very similar spatial structure with lidar, where data are measured on a cone with only the line of sight velocity component measured, and the resolution of data becoming higher closer to the instrument, due to shorter arclength of neighboring beams at small radius. In the meantime, Sawada et al. (2015) developed assimilation techniques for high-resolution data in limited domain suitable for lidar, using the Japan Meteorological Agency Nonhydrostatic Mesoscale Model.

At HKIA, long-range lidars are employed to detect low-level wind shear in dry weather (Shun and Lau 2002; Shun and

Chan 2008; Chan and Lee 2012). Operationally, plan position indicator (PPI) and range–height (RH) scans are constantly measured and are available in short time intervals (about 2.5 min) and short range gates (spatial resolution of 100 m along the radius of the lidar beam). The maximum range of these lidar is variable, depending on ambient conditions as well as user-defined settings, but in the fair weather cases the radial coverage is roughly 7 km, as compared with the coarser radar data resolution. This necessitates adaptation of data assimilation algorithms to incorporate such finescale observations for terminal wind forecasts.

Although both three-dimensional and four-dimensional variational data assimilation schemes (3D-var and 4D-var) are available in WRF, because of the prohibitive computational cost associated with cycling data assimilation, only 3D-var is considered here. The rest of the paper is organized as follows: in section 2, the adaptation of WRF 3D-var for cycling data assimilation in a high-resolution topography model near HKIA will be discussed; in section 3, through several cases, the results of the WRF 3D-var will be demonstrated; in section 4, using LCS, terrain-induced flow features will be contrasted among different extraction schemes and against actual flight data from pilot reports; and section 5 offers further discussion and conclusions.

2. WRF Model settings and lidar data assimilation

The numerical data assimilation is conducted using the Advanced Research WRF Model, version 4.0. WRF is a non-hydrostatic, primitive equation, mesoscale meteorological model with advanced dynamics, physics, and numerical schemes (Skamarock et al. 2019). In this study, WRF was run using six nested domains with two-way feedback. (Both one-way and two-way feedback schemes were initially tested and showed negligible difference; we nevertheless used two-way feedback as the default in later simulations.) The innermost nest had a grid spacing of 150 m while the largest had a grid spacing of 36.45 km, which corresponds to a parent–child grid ratio of 3. There are two lidar stations at HKIA. The innermost nest was centered at 22.313°N, 113.92°E, the coordinates of the northern lidar at HKIA, and had 157 grid points in both the x and y directions. It covered an area of 23.4 km \times 23.4 km. The remaining nests each had 133 grid points in the x and y directions. Eighty-five vertical levels were used, with a uniform spacing of about 15 m for the first 600 m of height, and then increasing in a nonlinear profile typical in WRF. The uniform spacing near boundary was chosen to try resolve the flow within the lidar range.

In terms of physical parameterizations, this study considered the new Thomson et al. scheme for microphysics, the Rapid Radiative Transfer Model (RRTM) scheme for both short-wave and longwave radiation, the Monin–Obukhov surface layer scheme and the Noah land surface model for surface physics, the Yonsei University scheme for boundary layer parameterization, the Tiedtke scheme for cumulus parameterization, and the Smagorinsky closure for eddy coefficient. In the innermost, sixth nest, because of the high resolution, no boundary layer or cumulus parameterization was used.

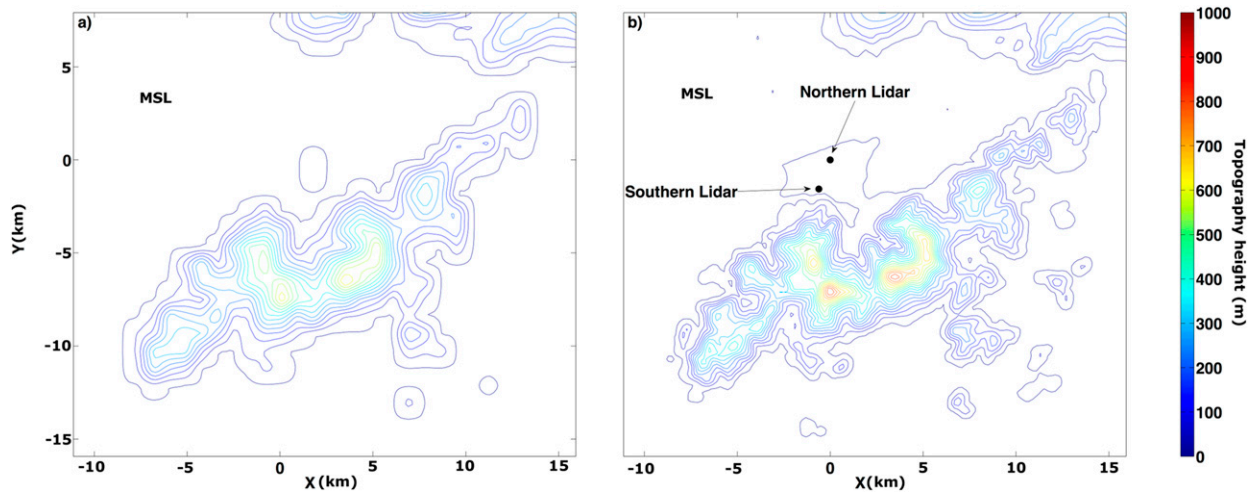


FIG. 1. A comparison of the topography of Lan Tau Island in the innermost WRF nest: (a) WRF Model topography, using 30 arc s topography data. (b) WRF Model topography, using ASTER 1 arc s topography data. Locations of the two long-range lidars are also shown in (b). The simulation is centered at the location of the northern lidar.

The 1.5-order TKE closure was chosen for the eddy coefficient. The initial conditions and boundary conditions for the outermost nest were driven by the NCEP FNL Operational Global Analysis data, which are available every 6 h on a $1^\circ \times 1^\circ$ grid resolution.

Since turbulence along the landing corridor is largely terrain driven, further consideration of the model topography is needed. The highest-resolution topography data included by default in WRF have a resolution of 30 arc s, which is roughly about 900 m around HKIA. Since the finest nest had a grid spacing of 150 m, a higher resolution of topography is needed. The Advanced Spaceborne Thermal Emission and Reflection Radiometer Global Digital Elevation Model (ASTER DEM) data are thus used, which provide terrain resolution at every 1 arc s (about every 30 m). Figure 1 shows the effects of making this change. Figure 1a shows the default WRF Model topography near HKIA using the 30 arc s data, and Fig. 1b shows the WRF Model topography using the ASTER 1 arc s data. As an example, the highest peak on Lan Tau Island south of the airport is about 934 m. Using the default 30 arc s topography results in an in-model peak of 655 m, whereas using the ASTER 1 arc s data result in an in-model peak of 860 m, which is much closer to the true value. This study is committed to a finer resolution of topography to capture terrain features matching lidar resolved flow patterns. Correcting the forecast with data that do not have, in any manner, their driving mechanism resolved in the model (i.e., from finescale topography) would likely result in only transitory changes where the forecast updates cannot be sustained between cycles. Accordingly, temporal resolution has been adjusted from the WRF default across all nests to maintain numerical stability with such a high spatial resolution of topography. For example, at the innermost nest, the time step is chosen to be about 0.12 s, roughly 1/8 of the default time stepping.

Because of the high temporal resolution to ensure numerical stability, the computational cost of these simulations is relatively

high. Using a workstation equipped with an eight-core CPU, the clock time is 3 min per 10 s of simulation, so a scaleup of at least ~ 20 times is necessary to bring the WRF simulations in real time, not considering overhead cost across different nodes and the time to perform each step of data assimilation (which is short). However, these exploratory simulations were pushing the extreme, and the settings could be relaxed. With a powerful cluster or workstation, real-time forecast should be attainable.

The two lidar stations are shown in Fig. 1b as the two black dots. The northern lidar, located at (0,0) in the domain, conducts PPI scans at an elevation of both 1.4° and 3.0° , whereas the southern lidar scans at 3.0° . Because of the closer proximity of the southern lidar's scanning cone to the mountains on Lan Tau Island, it is found that the northern lidar data generally provided superior results in the assimilation. As such, observations from both the scanning angles produced by the northern lidar are used in the assimilation, since a typical airplane landing trajectory lies between the two scans. The lidar data are provided from HKIA on a grid with 100-m spacing. WRFDA requires radar observations to be input with latitude/longitude coordinates to three decimal places. With these high-resolution lidar data, distinct data points sometimes had identical rounded coordinates. As such, direct assimilation of radial grid-based lidar data is not practical. The lidar data are interpolated onto WRF simulation grids to resolve such conflicts. Anomalous data (clutters) have been masked out before input into WRFDA. Depending on weather conditions, this ranged from relatively few data points to a majority of the data. Typically, though, around 5100 lidar observations were assimilated at each step. Updated lidar data were available for each elevation angle around every 140–150 s. Note that each complete lidar scan is regarded to be an observation at a single instance in time, whereas in reality, data at different azimuthal angles are observed at different times.

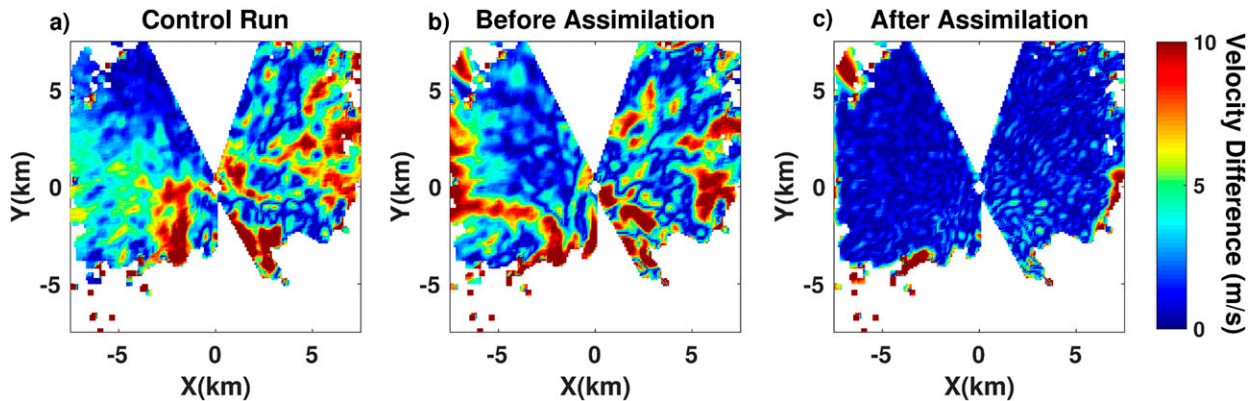


FIG. 2. The magnitude of the difference in radial velocity between WRF and the 3.0° lidar at 1342:40 UTC 19 Apr 2008 for (a) no data assimilation, (b) prior to assimilation at 1342:40 UTC [assimilation was performed at 1340:10 UTC (3.0°) and 1341:30 UTC (1.4°)], and (c) after data assimilation was performed at 1342:40 UTC (3.0°).

Key components of variational data assimilation are the background and observation error statistics. WRFDA allows for the creation of background error statistics particular to the domain under consideration or the use of a default statistics file; the default statistics information (the NCEP background model) is chosen in this study to apply to cases in different seasons and weather conditions. High trust is also given to the lidar data by restricting the observation error statistics. WRF automatically removes observations that cause too large an innovation. This feature was turned off since it may discard important features in the lidar observations. It is noted that recent studies show that observation error correlations can be significant and has been overlooked in NWP models (Miyoshi et al. 2013; Fowler et al. 2018). If the sign of the observation–operator coefficient and the observation–error correlations was different, accuracy of observation in state space at different scales may be affected. Thus, more careful consideration of the background and observation error statistics would be worthwhile in any operational implementation.

The cycling assimilation scheme is applied at every time instance when lidar PPI scan data are available (range height scans are not considered in this study). The output from WRFDA is taken to be the new WRF input file for that nest and drive the simulation until the next assimilation time. Since the lidar data are localized near HKIA, data assimilation is only performed on the innermost nest. Nest feedback is the only route by which the lidar information propagates to the other nests, although this feedback only has minor effects on the outer nests due to the limited range of the lidar observations.

3. Results from WRFDA

While data assimilation techniques have been implemented to study the flow near HKIA from radar and lidar data, the results are mostly in the form of postanalyses, in the sense that they have not been used as new initial conditions to drive NWP models in forecasts. The work in this section develops such capabilities in the WRF platform, which both serves as a forecasting tool, and as the basis for the subsequent Lagrangian analyses.

Four different case studies on two separate days, 19 April 2008 and 21 February 2009, were analyzed to test the data assimilation procedure described above, and used in the subsequent Lagrangian analyses in section 4. The days and times were chosen to correspond to available flight data. To illustrate the error propagation over time and space, WRF simulation with no data assimilation is used as the control run and the LOS velocity from lidar is considered the ground truth in this section. Effectiveness of data assimilation is reflected by the reduction of error between the WRF Model outputs and the lidar measurements. For all cases, both 1.4° and 3.0° scans from the northern lidar are assimilated, at the times when they become available. Cycling started at a given time of interest, and ran through a 10-min period, covering a certain landing event (to provide sufficient data for Lagrangian trajectory integration). Within each of such period, a total of 8–9 PPI scans are incorporated. Two such cases are presented in this section.

a. 19 April 2008

A tropical cyclone made landfall and moved inland, causing strong southerly winds on 19 April 2008. WRF was spun up starting at 1200:00 UTC and run until the assimilation cycling started at 1340:10 UTC. Figure 2 shows comparison between the lidar and WRF radial velocity, in terms of its magnitude, without and with data assimilation, at 1342:40 UTC. Figure 2a shows the error in the control run. Data assimilation is effective if it reduces this error while maintaining the resolved velocity field physically relevant. At this point in time, 3D-var has gone through two assimilation cycles, one step at 1340:10 UTC, using lidar data at the 3.0° PPI scan, and another at 1341:30 UTC, using lidar data at the 1.4° PPI scan. The error between lidar and 3D-var before the next assimilation step is shown in Fig. 2b. The error between the two immediately after the assimilation step, using lidar data at the 3.0° PPI scan, is shown in Fig. 2c. First, Fig. 2c is representative of the LOS velocity error between WRFDA and lidar immediately after any assimilation step, with magnitude of error within $\sim 3 \text{ m s}^{-1}$ in the interior, and maximum error confined at the edge of the lidar domain (thus can be thought of, qualitatively, as the assimilation taken

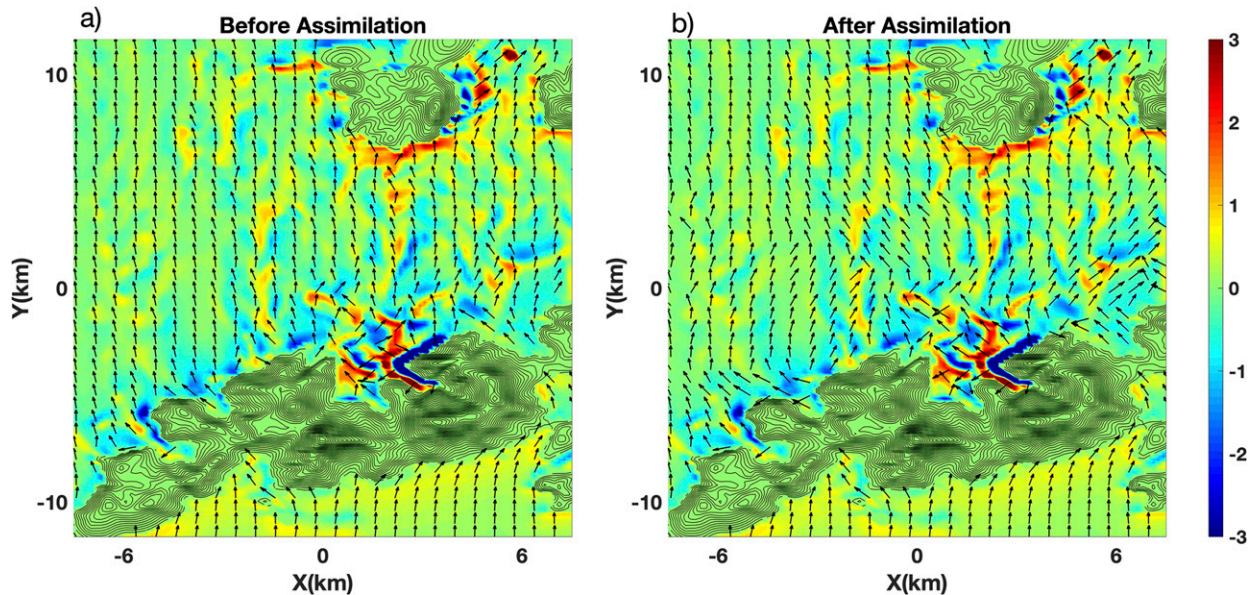


FIG. 3. Vector plots of the horizontal wind velocity, with a color plot of the w component in the background, at 100 m MSL, at 1340:10 UTC 19 Apr 2008 (a) before assimilation and (b) after assimilation.

1340:10 UTC, not shown). After continuation of simulation in WRF, the error magnitude will grow. In this particular case, after 150 s, the growth of error is still better than WRF without data assimilation, especially around the lidar and along the landing corridor toward the east. After the next assimilation step using the new 3.0° data, the error gets controlled again.

It is important to point out that since the lidar observations are range limited, the improvements do not last very long, as evidenced by the quick growth of errors. However, continuous assimilation helps mitigate the lack of memory from the model. We also note that as explained in Sawada et al. (2015), limited area models, such as the high-resolution HKIA model we consider here, are strongly influenced by lateral boundary conditions. Implementation of lateral boundary adjustment may help the forecast to stay closer to observations longer. Sawada et al. (2015) considered emulated lidar data available at every 15 min, and was able to generate forecast out to 1 h, or four assimilation steps. This is consistent with our setting, since within 10 min, each PPI angle has been assimilated four times, for a total of 8–9 scans between the two PPI angles. However, in the emulated lidar data, Sawada et al. (2015) considered 20 elevation angles, which makes the observations much denser than our operational scans. This may yield some differences when implementing lateral boundary adjustments.

Changes in the flow due to data assimilation are shown in Fig. 3 to indicate its physical relevance. In Fig. 3a, the horizontal velocity vectors, as well as a color contour of the vertical velocity w , are at the level of 100 m above mean sea level (MSL), before the assimilation step at 1340:10 UTC. The result immediately after assimilation is shown in Fig. 3b. As seen, the assimilation did not change too much of the vertical velocity in this case, but it does change the horizontal velocity vectors immediately north of the Lan Tau Island. Effectively, locations of convergence and divergence of velocity vectors have changed,

and the consequence of these changes are reflected in the Lagrangian analyses in section 4.

b. 21 February 2009

A high pressure ridge was over the southeastern coast of China on 21 February 2009, which caused strong easterly winds at HKIA, with rain affected the range of the lidar throughout the course of the day. WRF was spun up starting from 0600:00 and run until 0750:10 UTC, when data assimilation using 3D-var was started. Figure 4 shows the difference between the lidar and WRF radial velocity, without and with data assimilation, at 0751:10 UTC. Similar to Fig. 2, Fig. 4a shows the error in the control run. At this point in time, 3D-var has gone through one assimilation cycle, at 0750:10 UTC, using lidar data at the 3.0° PPI scan. The error between lidar and 3D-var before the next assimilation step is shown in Fig. 4b. The error between the two immediately after the assimilation step, using lidar data at the 1.4° PPI scan, is shown in Fig. 4c. It is interesting to note that, in Fig. 4b, after continuing WRF using assimilation at a different elevation, the error is relatively small, indicating that the dynamics changed from 3.0° PPI scan is consistent with the physics at 1.4° . This also affirms the assimilation strategy using both scanning angles—incorporating data from one elevation angle will not adversely affect the assimilation in the other elevation angle.

Similar to the comparison in Fig. 3, the changes in the flow are shown as velocity vector plots in Fig. 5, at 0750:10 UTC. As before, Fig. 5a shows the WRF Model without assimilation, Fig. 5b shows the result of data assimilation. The vectors show horizontal wind directions at 100 m MSL and the color contour shows vertical velocity at this elevation. There are some immediate features to note in this comparison. First, the direction of the flow has changed subtly, with a more northward tendency than the base WRF Model around HKIA. Second, the data

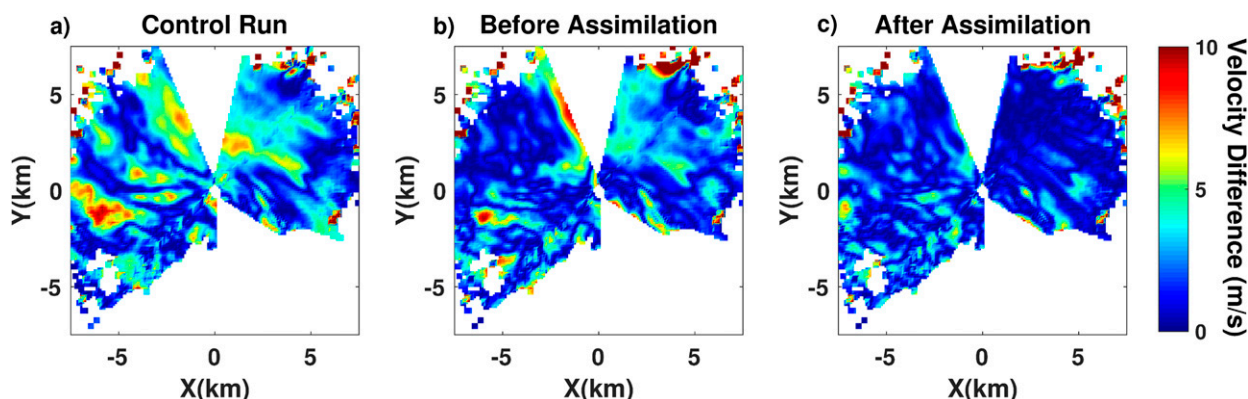


FIG. 4. The magnitude of the difference in radial velocity between WRF and the 1.4° lidar at 0751:10 UTC 21 Feb 2009 for (a) no data assimilation, (b) prior to assimilation at 0751:10 UTC [assimilation was performed at 0750:10 UTC (3.0°)], and (c) after data assimilation was performed at 0751:10 UTC (1.4°).

assimilation has resulted in a region of very strong vertical motion to the east of Pui To Shan, due north of HKIA. There now appears to be a back flow as the air hits the landmass, rather than being carried directly over in the WRF control run. This may be a result of the slight change of the flow direction after data assimilation, better matching the radial velocity with the lidar. Third, the complex flow structures in the region to the west of HKIA has been changed, both in horizontal structure and vertical speed, indicating that along the landing corridor the WRFDA model may now yield structures that match better with those produced by lidar.

4. Comparisons of LCS and onboard flight data

The Lagrangian trajectories of air parcels are integrated based on the velocity data from 2D-var, WRF, and 3D-var to generate LCS for comparison among the three datasets, and

with vertical acceleration measured on board landing flights. Using two-dimensional velocity on the lidar scanning cone, either from 2D-var, or using velocity projected on the lidar cone using WRF and 3D-var data, the FDFTL method developed in Tang et al. (2010) is employed to obtain LCS. Note that although the results in Knutson et al. (2015) indicate that emulating a 2D-var using three-dimensional model data produces results closest to the lidar-based 2D-var LCS, there is no point in doing so here, because 3D-var already incorporates lidar data, and as explained below, 2D-var is not the benchmark in this section. Trajectory integration time is 5 min, consistent with those used in previous studies. Note that, as argued in Tang et al. (2011a,b), ridges in the forward-time FTLE indicate separation, and should generally correspond to vertical downdrafts, hence a negative vertical acceleration measured on board the aircraft, whereas a backward-time FTLE ridge should generally correspond to a vertical updraft,

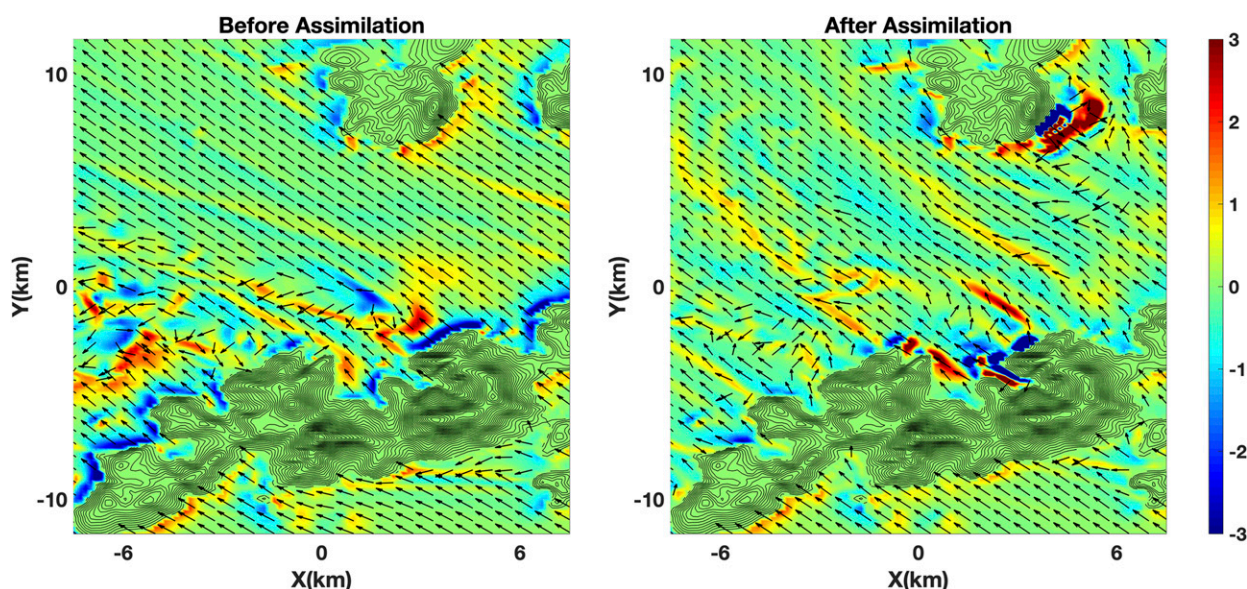


FIG. 5. As in Fig. 3, but at 0750:10 UTC 21 Feb 2009.

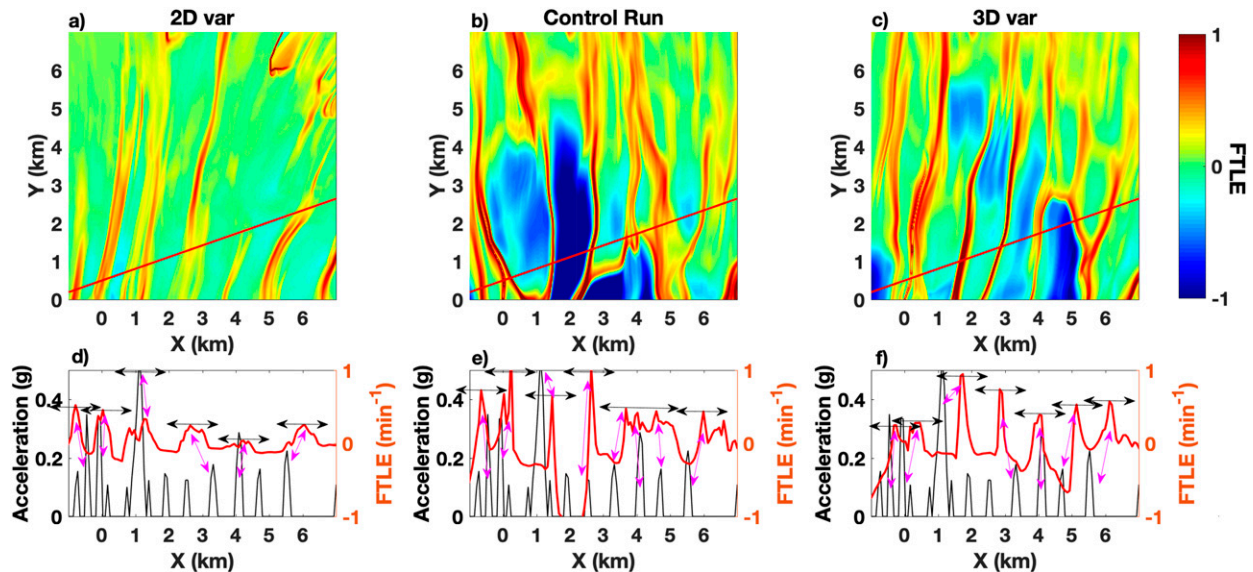


FIG. 6. Comparison of LCS among (a),(d) 2D-var; (b),(e) WRF control run; and (c),(f) WRF 3D-var for a missed approach at 1346:40 UTC 19 Apr 2008. The backward-time FTLE is shown in (a)–(c), highlighting structures responsible for updrafts. The red straight line in (a)–(c) indicates the landing path, from east of the airport toward west. Interpolation of FTLE along this path is shown in (d)–(f), in red, and is compared with onboard measurement of vertical acceleration, in black. Local peaks in FTLE, if within 800 m of an onboard-measured updraft, are paired with the updrafts using the magenta double arrows. Black double arrows mark the 800-m radius from FTLE peak to consider correlation.

that is, a positive vertical acceleration measured on board. For the cases considered, the predominant wind comes from Lan Tau Island and propagates downwind toward water. As such, Lagrangian trajectories in backward time shows more significant instabilities than those in forward time. Since missed approaches studied here typically associate with updrafts, and forward-time FTLE are less significant over the water, only comparisons with backward time FTLE fields are shown.

a. 19 April 2008

On 19 April 2008, a missed approach occurred at 1346:40 UTC at HKIA, and the airplane landed safely later. As a benchmark case, this landing has also been studied previously, but only with 2D-var results (cf. Fig. 8 in Tang et al. 2011b). The WRF and 3D-var analyses are performed now to reveal new analyses of this case. Trajectory integration started at 1345:40 UTC, in backward time, for 5 min.

Around this time, a 1.4° PPI scan is available. Figure 6 compares the coherent structures obtained at this time, along with vertical acceleration measured on board the flight. The color contours are the backward-time FTLE fields generated from Fig. 6a 2D-var, Fig. 6b WRF control run, and Fig. 6c WRF 3D-var. In each panel, the red line indicates the landing path of the aircraft. In Figs. 6d–f, the backward-time FTLE is interpolated along the landing flight path (red) and compared with onboard measurements of vertical acceleration (black). Figure 6d corresponds to the 2D-var FTLE, Fig. 6e the WRF FTLE, and Fig. 6f the WRF 3D-var FTLE. To highlight major jolts felt on board and help to establish correlation, vertical acceleration less than 0.1 g has been set to 0.

It is noted that both WRF cases yield LCS more complex than the lidar. In comparing the LCS in the top three panels, it is seen that the WRF control run, in Fig. 6b, shows structures oriented north–south, whereas the 2D-var, in Fig. 6a, yields structures oriented more to the northeast. As Fig. 6c shows, the 3D-var is successful in aligning the flow structures to match the 2D-var LCS. It is important to point out that, the 2D-var LCS cannot be treated simply as the ground truth. Both 2D-var and 3D-var had velocity information inferred transversal to the LOS direction, hence there is only partial truth. However, it is also worth pointing out that the 2D-var and 3D-var minimize different cost functions, so similarity between 2D-var and 3D-var shows a certain consistency between the two retrievals.

The fact that 2D-var and 3D-var give rise to similar structures makes one wonder if information from 2D-var alone is already good enough, that is, if the extra cost of running WRF and 3D-var is worthwhile. Indeed, it can be seen that the extra cost of running WRF is also beneficial, because the full dynamics in three-dimensional flow is properly resolved. One immediate consequence is that conservation of mass in three dimensions allows trajectories to separate further (as compared to 2D-var where conservation of mass is only along the scanning cone), thus highlighting instabilities, leading to more pronounced peaks in the FTLE plot. This is seen both in Figs. 6b and 6c, from three-dimensional flows, where the color map show more variation from maxima to minima as compared to Fig. 6a. As such, LCS from the three datasets are of equal significance: 2D-var emphasizes observation, and the WRF control run emphasizes physics; WRF 3D-var, being the hybrid between realistic dynamics and matching observations, is likely to produce balanced results.

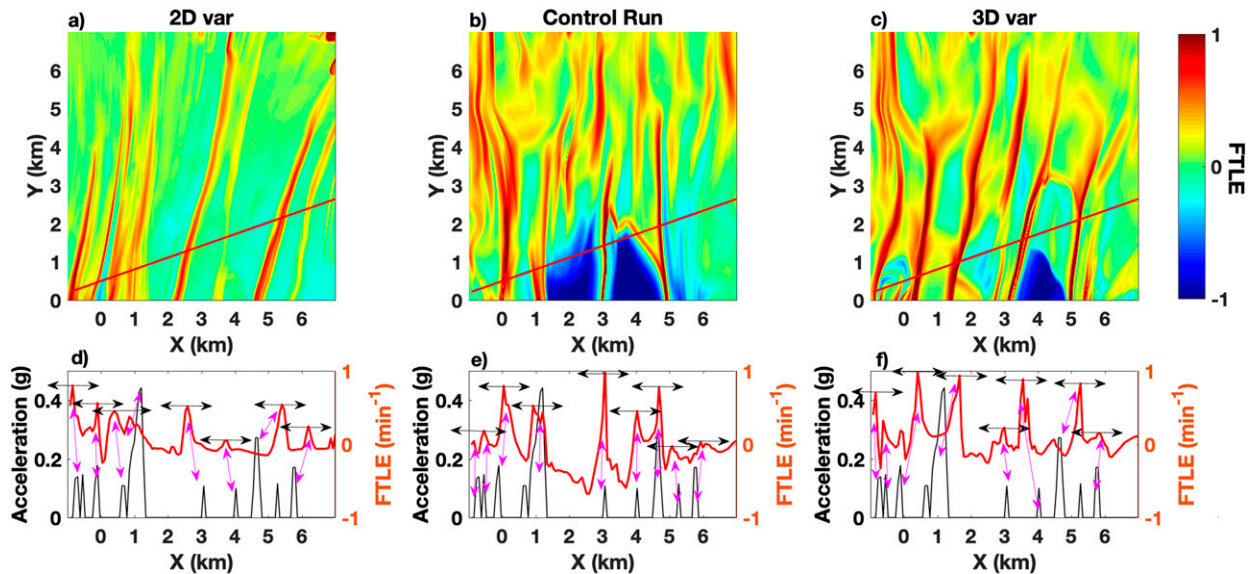


FIG. 7. As in Fig. 6, but for a missed approach at 1403:40 UTC.

In this regard, the only truth to consider and compare to LCS is the vertical acceleration recorded from onboard sensors. The quality of the LCS is then in terms of how well they compare to the pilot reports. Because the lidar and the onboard sensor are two independent instruments, measuring different quantities of the same airflow at slightly different times, and the subsequent processing of data takes into account many modeling assumptions, it is very demanding to require a precise match between FTLE and acceleration peaks.

Considering the updrafts measured on board (among the four cases), roughly 10 spikes can be found to exceed 0.1 g over a distance of 8 km. We thus consider a radius of 800 m to seek correlation between the FTLE peak and updraft peak. Roughly speaking, the highest updraft peak within 800 m left or right of the FTLE spike is considered to be correlated to the FTLE spike, unless it is already paired with a larger FTLE spike. Eight hundred meters corresponds to the detected location to be within 10 s of true updraft locations, it is also smaller than the average gap between major FTLE spikes. Note that the 0.1 g and 800 m thresholds are highly subjective; the pairing results may change subject to these choices. We made these choices to optimize proximity and magnitude as well as patterns of the peaks among the cases analyzed.

As an example, by requiring that the FTLE peak to be within 800 m of acceleration peak, regardless of the magnitude of the peak, roughly 6 peaks in acceleration can be accounted for using 2D-var, shown in Fig. 6d). In Fig. 6d, the black double arrows indicate a radius of 800 m from the local peak, and the magenta double arrows indicate possible matches between FTLE and sensor measured peaks. It can be noted that there might be multiple FTLE peaks near a measured updraft. For example, the acceleration peak near 1 km from lidar could be due to either of the two peaks nearby. Furthermore, the acceleration peak around 4 km seems to associate with a rather weak FTLE peak, making the identification of this peak solely

from 2D-var FTLE questionable—if a slightly restrictive criterion is selected, such as FTLE or its gradient to exceed some modest value, this peak cannot be identified (since sensor data are measured at the time and location of air disturbance, and cannot be used as warning for the aircraft ahead of time). However, the peak at 4 km registers the second largest acceleration along the flight path.

While the distinct peak in vertical acceleration at 1 km east of lidar is near two FTLE peaks in 2D-var, the FTLE magnitude is not much larger than the other two FTLE peaks around 3 and 6 km. It is unknown if this particular updraft has led to the missed approach, but the airplane pulled up around this location [not shown; the interested reader is referred to Fig. 8f in Tang et al. (2011b)]. For a successful detection method, one would hope to at least identify distinguished peaks existing along the flight path, within the last 5 min of landing [in the spirit of Fawcett (2006) and Kafiabad et al. (2013)], if not able to pinpoint where those peaks are located. It can be seen that WRF and 3D-var results in Figs. 6e and 6f do offer such distinguished features. In Figs. 6e and 6f, the major peaks have much larger net jump, making them easily identifiable (gradient is not used here to avoid twin spikes associated with the two sides of one FTLE peak). Between WRF and 3D-var LCS, it can be seen that 3D-var has more isolated peaks, corresponding more or less to the location and number of the acceleration peaks, and the largest FTLE peak can be paired with the true acceleration peak. In comparison, the peak near 1 km for WRF LCS is not the largest peak, and the structures between 3 and 5 km in Fig. 6e are not as distinguished. From this one case, 3D-var appears to be more advantageous in identifying flow hazards.

In Fig. 7, the same LCS analyses is applied to a missed approach at 1403:40 UTC 19 April 2008. All layouts are the same as Fig. 6. In this case, there is a major updraft at 1 km from the onboard sensor. The 2D-var LCS in Fig. 7d does have peaks around 1 km, very close to this updraft. It also identifies a few

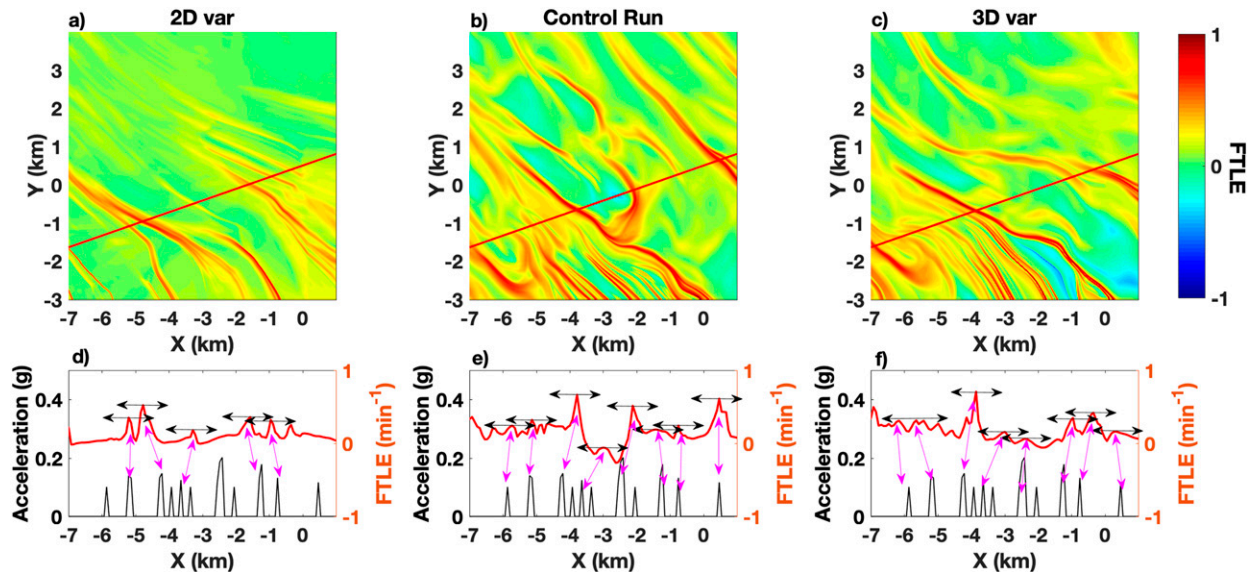


FIG. 8. As in Fig. 6, but for a successful approach at 0752:20 UTC 21 Feb 2009. Note that the change in wind direction makes the landing path from west to east.

other peaks farther away from the lidar. Figure 7e, on the other hand, does reveal more FTLE peaks, and many are well aligned with vertical acceleration almost precisely in location. However, the peak associated with the major draft has a weaker FTLE peak, as compared to a major FTLE peak at 3 km, associated with a rather minor acceleration peak. The FTLE does reveal the secondary acceleration peaks very well. On the other hand, the 3D-var LCS revealed in Fig. 7f produce similar peak to peak correspondence, with the peak locations slightly worse than the WRF control run, but the largest FTLE peak is within 800 m of the corresponding acceleration peaks. For this case, while the correspondence of location of the peaks is about the same among the three datasets, 3D-var is better than 2D-var for being more distinguished, and slightly better than WRF control run in the capability to detect the largest updraft with the tallest FTLE peak.

b. 21 February 2009

Figure 8 corresponds to a successful landing at 0752:20 UTC 21 February 2009. Note that the changing wind direction makes landing aircraft approach from the west. In this comparison, we first note that WRF and 3D-var produce more complicated structure than 2D-var, similar to the cases on 19 April 2008. Direct comparison of the FTLE interpolated along the flight path with the vertical acceleration from onboard sensors, in Figs. 8d–f, indicate that there is no major updraft in this case, and thus the airplane landed safely. Correspondingly, the FTLE peaks are not as significant, especially in the 3D-var-based LCS. The WRF control run shows a larger jump than 3D-var near –3 km in Fig. 8e, although this jump is not as significant as the ones in Figs. 6 and 7 indicating strong updrafts. The 2D-var-based LCS does not have large peaks, but the peak magnitude is not much smaller than those seen in Figs. 6 and 7, which has correspondence with significant

updrafts, making an FTLE-based metric difficult, if directly obtained from 2D-var. For WRF and 3D-var, since the peak magnitude is roughly below 0.7 min^{-1} , a threshold above this peak magnitude may successfully identify this case as safe landing condition.

As one last case, Fig. 9 corresponds to a missed approach at 0837:40 UTC 21 February 2009. There is a major updraft occupying between –2 and –1 km to the west of lidar, with a peak around –1.5 km. There are a few other minor peaks farther away from lidar. Comparing Figs. 9d–f, it can be seen that the 2D-var LCS in Fig. 9d does pick up a major peak around –1 km, and a secondary peak at around –5 km. The WRF-based LCS in Fig. 9e picks up peaks at –3 and –0.5 km, with a series of secondary peaks to the west of –3 km. In comparison, the 3D-var-based LCS in Fig. 9f picks up a major peak at about –0.5 km, along with a series of smaller peaks to the west of –3 km. In this case, while 2D-var pick up a major updraft from FTLE, overall, the 3D-var-based LCS appears to capture the true trend of the acceleration peaks as revealed in the black curve (a series of small updrafts to the west of lidar, followed by a major updraft around –0.5 km west of lidar). Here, we make an exception to the 800-m-radius pairing rule. There is only one major updraft around –1.5 km measured on board. In the 2D-var LCS it is paired to a FTLE peak at about –1 km. Judging from the 2D FTLE structures in Figs. 9a–c, it can be inferred that this peak is moved to –0.5 km for WRF and 3D-var cases. We thus still pair the FTLE peak at –0.5 km, with the updraft at –1.5 km, even though it is slightly beyond our original protocol. The pairing is indicated by the blue double arrow in Figs. 9e and 9f.

We note that, the practical goal of the development of Lagrangian detection tools is to hopefully capture the major wind shear events relevant to wind hazards near the airport. The capability of LCS to correspond to major jolts in unsuccessful

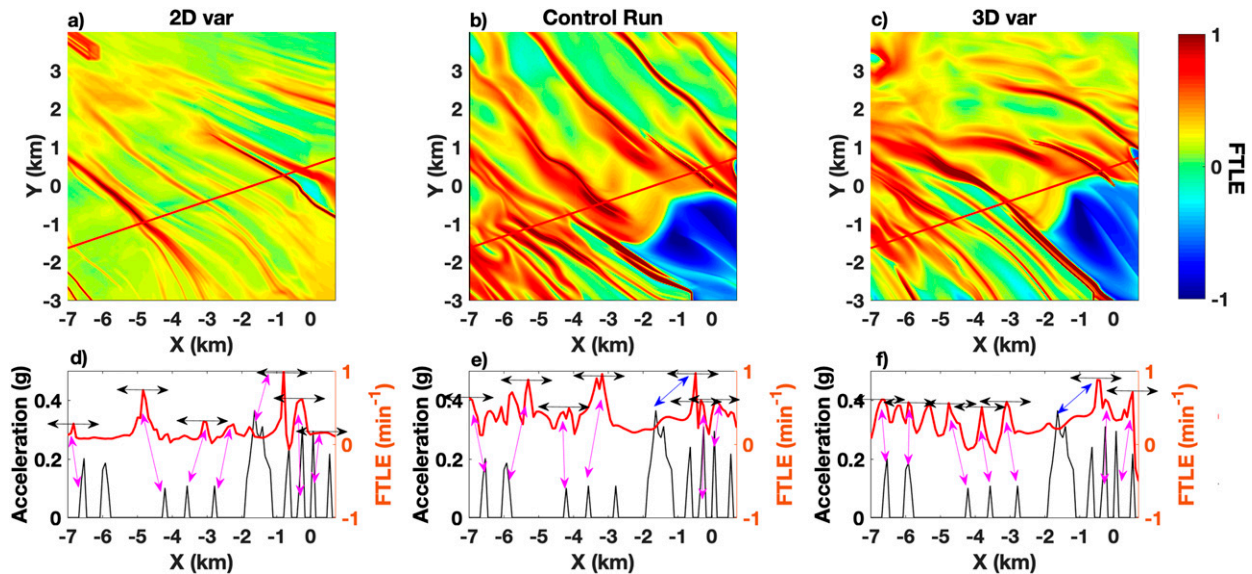


FIG. 9. As in Fig. 8, but for a missed approach at 0837:40 UTC 21 Feb 2009.

landings may be attributed to averaging along Lagrangian trajectories, filtering out transient errors and highlighting true, significant signals (the wind shear is so pronounced that modeling and measurement errors do not affect it being revealed). Minor peaks are more prone to these errors and correspondences may not be as clear to establish. However, with only four preliminary cases considered here, we cannot pinpoint a robust threshold distinguishing between “major” and “minor” peaks in the FTLE field that are hazardous/safe to flight operations. Inspecting among the three unsuccessful landings, a common trend is an updraft exceeding 0.2g (where g is the gravitational acceleration) within 2 km of the lidar. It is unknown if these particular updrafts caused the turnaround, but we are able to locate major peaks of FTLE in close proximity to pair with these updrafts. In comparison, the highest FTLE peak in Fig. 8 is not in close proximity with the largest updraft for the successful landing case.

In Chan (2012), when comparing the F factor between those measured on board and those estimated from lidar, the largest peaks between the two sets of data are compared, regardless of proximity (as long as they both are inside the 4 n mi range from runway thresholds), using 300 flights. Here we attempt to make a similar calculation, both using the peak–peak correspondence within the domain we consider, and the paired correspondence, considering proximity. The results are shown in Fig. 10. In all panels, the horizontal axes correspond to updraft peaks, the vertical axes correspond to FTLE peaks. The left column is computed from 2D-var, the center column from control run and the right column from 3D-var. We seek to minimize the variance in the scatter by a least squares fit to a linear line; the results are shown as the black straight lines. Using the same strategy of Chan (2012), we only have four data points. The results are in the top row. It is apparent that 2D-var FTLE peak is unable to explain the variance in magnitude of updraft. The control run almost have a R2 value of 1, meaning that using just WRF, the peak to peak relation is capable to explain all the variability in the maximum updraft. The

R2 value using data from 3D-var is 0.81, not too much less than WRF. In comparison, the R2 in F-factor peaks in Chan (2012) was around 0.7. However, we stress that this result only contains four data points, and the FTLE-updraft peaks are not necessarily in close proximity to each other.

When strictly following the rule to generate pairs in close proximity, the R2 value decrease dramatically, likely due to the various sources of errors when wind shear is weak. In this case, considering around 30 pairs in each panel, the 2D-var result is still not very relevant (in terms of magnitude). The R2 in 3D-var is much better than WRF, even though neither is greater than 20%. This clearly indicates that a threshold to distinguish “major” and “minor” peaks is necessary to improve the R2 in any of the fittings. As such, further validation is necessary through statistical studies among larger datasets, similar to Kafiabad et al. (2013), to test and optimize all the subjective thresholds as proposed here.

5. Conclusions

Data assimilation (DA) of lidar scans at HKIA using 2D-var and 3D-var have been performed. Lagrangian coherent structures (LCS) based on the 2D-var, WRF control run, and 3D-var have been contrasted against vertical acceleration data measured on board flights. Turbulence at HKIA is largely terrain driven, thus high-resolution topography data were input into WRF, and very high spatial and temporal resolution have been employed. Based on two case studies from different weather conditions, it is found that the cycling data assimilation improved the WRF forecast to be closer to observations.

Comparing the LCS obtained from the three datasets, it is found that WRF and 3D-var improves hazard detection as compared with 2D-var approach developed in Tang et al. (2011a,b). Using the finite-domain–finite-time Lyapunov exponent as the diagnostic for vertical motion, the magnitude of 3D-var and WRF peaks correspond well to the severity of the updrafts, which is

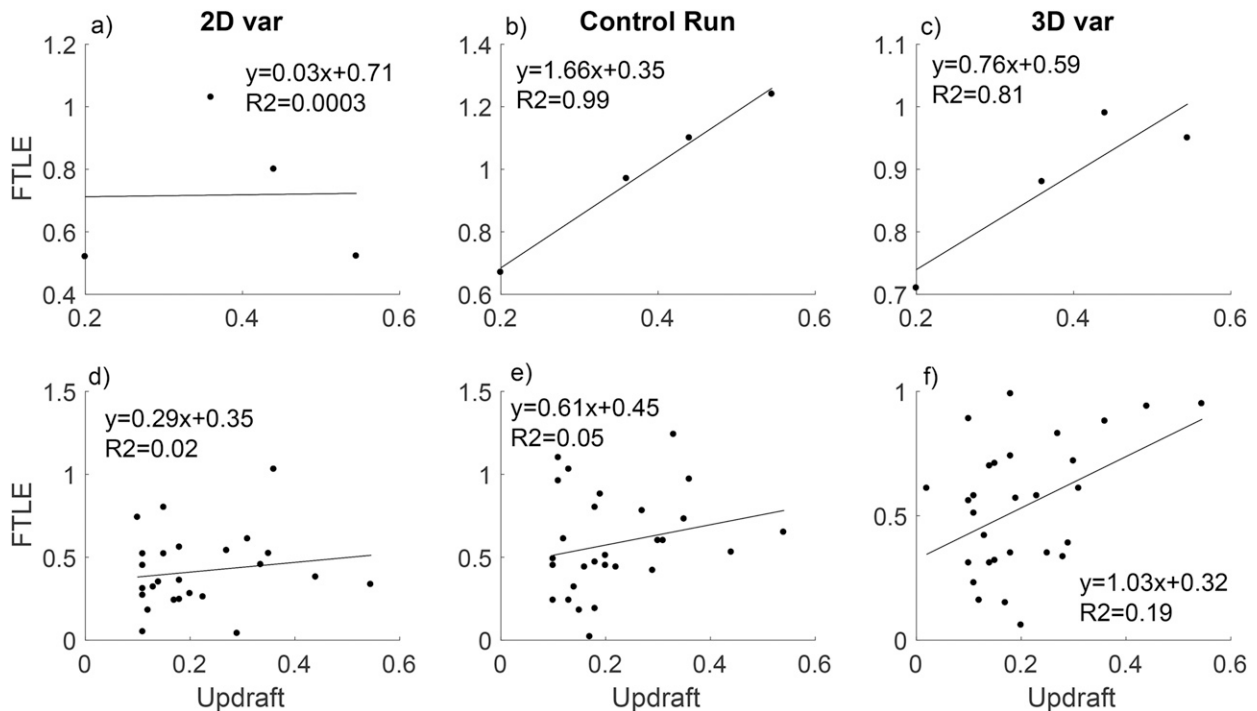


FIG. 10. Peak pairing statistics among all four cases. Scatterplot of paired FTLE peak against updraft peak. (a)–(c) Maximum updraft vs maximum FTLE along the glide path. (d)–(f) Paired updraft vs FTLE peak, as indicated in Figs. 6–9. The plots in (a) and (d) are computed using 2D var, those in (b) and (e) are computed using the WRF control run, and those in (c) and (f) are computed using 3D var. The black straight lines indicate the best linear fit among the scattered data. The R^2 value indicates how well the linear fit explains the variance seen in the updraft.

superior to 2D-var FTLE. It is also found, based on the four landing cases analyzed, that 3D-var FTLE is slightly superior to WRF FTLE in how isolated and how well the peaks correspond to true updrafts. This correspondence gives hope for using WRF or 3D-var FTLE as a refined metric to improve hazard detection.

There are many balances to consider for operational implementation of lidar DA in WRF. The detailed topography improved the base forecast but required a very small time step. Less detailed topography would produce a less accurate base forecast but would allow a larger time step. This larger time step, in turn, may even allow the use of 4D-var, instead of 3D-var, to incorporate lidar data for running the adjoint model in the analysis, which might result in an improved forecast to rival the high-resolution topography case. However, because the nearby topography is one major source of uncertainty in the forecast, reduction of resolution for the topography may lead to the loss of a generation mechanism for small-scale turbulence altogether, thus making the cycling DA oscillatory between feature incorporation from DA and subsequent loss due to low-resolution topography. Improvements could also potentially be made by generating domain-specific and season-specific background error statistics rather than using generic statistics, as well as considering lateral boundary adjustment.

There are different possible future applications for using these results to improve real-time wind shear detection. First, the 3D-var data could be used to generate detailed forecasts near HKIA, but a more scalable computational platform is needed to accommodate the cost. Second, for hazard detection based on

3D-var FTLE, a longer season analyses should be carried out, in a similar fashion to Kafiabad et al. (2013), to obtain the receiver operating characteristics and to validate this methodology as well as the specific threshold. In this study, based on the four cases considered, it appears that the FTLE peak values serve as a good indicator of updrafts. New criteria may be based on this magnitude as well as a weighted proximity of the updraft detection. Third, using the full three-dimensional wind data, one can generate a multitude of lidar observations, and using pattern recognition techniques, it is possible to train a program to analyze two-dimensional lidar LCS to infer the underlying three-dimensional structures, as done in Tang et al. (2011a), and identify possible wind shear events along the landing corridor.

Acknowledgments. Brent Knutson was partially supported from NSF Grant ATM-0934592. This paper is adapted from his Ph.D. dissertation, *Pattern Identification and Analysis in Urban Flows* (Knutson 2018, chapter 4), repeated for convenience of the reader.

APPENDIX

Namelist Variables

Some of the namelist variables in WRF that are relevant to domain, physics, and dynamics and their values are listed here for the convenience of the reader.

time_step	10
time_step_fract_num	0
time_step_fract_den	1
max_dom	6
e_we	133, 133, 133, 133, 133, 157
e_sn	133, 133, 133, 133, 133, 157
e_vert	85, 85, 85, 85, 85, 85
dx	36 450, 12 150, 4050, 1350, 450, 150
dy	36 450, 12 150, 4050, 1350, 450, 150
grid_id	1, 2, 3, 4, 5, 6
parent_id	1, 1, 2, 3, 4, 5
i_parent_start	1, 45, 45, 45, 45, 33
j_parent_start	1, 45, 45, 45, 45, 33
parent_grid_ratio	1, 3, 3, 3, 3, 3
parent_time_step_ratio	1, 1, 3, 3, 3, 3
mp_physics	8, 8, 8, 8, 8, 8
ra_lw_physics	4, 4, 4, 4, 4, 4
ra_sw_physics	4, 4, 4, 4, 4, 4
sf_sfclay_physics	1, 1, 1, 1, 1, 1
sf_surface_physics	2, 2, 2, 2, 2, 2
bl_pbl_physics	1, 1, 1, 1, 1, 0
bldt	0, 0, 0, 0, 0, 0
cu_physics	16, 16, 16, 16, 16, 16
cudt	5, 5, 5, 5, 5, 5
km_opt	4, 4, 4, 4, 4, 2
diff_opt	2, 2, 2, 2, 2, 2

REFERENCES

- Barker, D. M., W. Huang, Y.-R. Guo, A. J. Bourgeois, and Q. N. Xiao, 2004: A three-dimensional (3DVAR) data assimilation system for use with MM5: Implementation and initial results. *Mon. Wea. Rev.*, **132**, 897–914, [https://doi.org/10.1175/1520-0493\(2004\)132<0897:ATVDAS>2.0.CO;2](https://doi.org/10.1175/1520-0493(2004)132<0897:ATVDAS>2.0.CO;2).
- , and Coauthors, 2012: The Weather Research and Forecasting Model's Community Variational/Ensemble Data Assimilation System: WRFDA. *Bull. Amer. Meteor. Soc.*, **93**, 831–843, <https://doi.org/10.1175/BAMS-D-11-00167.1>.
- Carruthers, D. J., J. C. R. Hunt, and W. S. Weng, 1988: A computational model of stratified turbulent airflow over hills—FLOWSTAR I. *Computer Techniques in Environmental Studies*, P. Zanetti, Ed., Springer-Verlag, 481–492.
- Chan, P. W., 2009: Aviation applications of the pulsed Doppler lidar—Experience in Hong Kong. *Open Atmos. Sci. J.*, **3**, 138–146, <https://doi.org/10.2174/1874282300903010138>.
- , 2010: Lidar-based turbulence intensity calculation using glide-path scans of the Doppler light detection and ranging (lidar) systems at the Hong Kong International Airport and comparison with flight data and a turbulence alerting system. *Meteor. Z.*, **19**, 549–563, <https://doi.org/10.1127/0941-2948/2010/0471>.
- , 2012: Application of lidar-based F-factor in windshear alerting. *Meteor. Z.*, **21**, 193–204, <https://doi.org/10.1127/0941-2948/2012/0321>.
- , and A. M. Shao, 2007: Depiction of complex airflow near Hong Kong International Airport using a Doppler lidar with a two-dimensional wind retrieval technique. *Meteor. Z.*, **16**, 491–504, <https://doi.org/10.1127/0941-2948/2007/0220>.
- , and Y. F. Lee, 2012: Application of short-range lidar in wind shear alerting. *J. Atmos. Oceanic Technol.*, **29**, 207–220, <https://doi.org/10.1175/JTECH-D-11-00086.1>.
- , K. K. Hon, and D. K. Shin, 2011: Combined use of headwind ramps and gradients based on lidar data in the alerting of low-level windshear/turbulence. *Meteor. Z.*, **20**, 661–670, <https://doi.org/10.1127/0941-2948/2011/0242>.
- Choi, Y., G.-H. Lim, and D.-K. Lee, 2013: Radar radial wind data assimilation using the time-incremental 4D-Var method implemented to the WRFDA system. *Tellus*, **65A**, 19677, <https://doi.org/10.3402/tellusa.v65i0.19677>.
- Fawcett, T., 2006: An introduction to ROC analysis. *Pattern Recognit. Lett.*, **27**, 861–874, <https://doi.org/10.1016/j.patrec.2005.10.010>.
- Fowler, A. M., S. L. Dance, and J. A. Waller, 2018: On the interaction of observation and prior error correlations in data assimilation. *Quart. J. Roy. Meteor. Soc.*, **144**, 48–62, <https://doi.org/10.1002/qj.3183>.
- Haller, G., 2001: Distinguished material surfaces and coherent structures in three-dimensional fluid flows. *Physica D*, **149**, 248–277, [https://doi.org/10.1016/S0167-2789\(00\)00199-8](https://doi.org/10.1016/S0167-2789(00)00199-8).
- Hon, K. K., and P. W. Chan, 2014: Application of lidar-derived eddy dissipation rate profiles in low-level wind shear and turbulence alerts at Hong Kong International Airport. *Meteor. Appl.*, **21**, 74–85, <https://doi.org/10.1002/met.1430>.
- , Y. Y. Chiu, and W. Tang, 2014: Application of short-range lidar in early alerting for low-level windshear and turbulence at Hong Kong International Airport. *Adv. Meteor.*, **2014**, 162748, <https://doi.org/10.1155/2014/162748>.
- Huang, X.-Y., and Coauthors, 2009: Four-dimensional variational data assimilation for WRF: Formulation and preliminary results. *Mon. Wea. Rev.*, **137**, 299–314, <https://doi.org/10.1175/2008MWR2577.1>.
- Kafiabad, H. A., P. W. Chan, and G. Haller, 2013: Lagrangian detection of wind shear for landing aircraft. *J. Atmos. Oceanic Technol.*, **30**, 2808–2819, <https://doi.org/10.1175/JTECH-D-12-00186.1>.
- Knutson, B., 2018: Pattern identification and analysis in urban flows. Ph.D. dissertation, Arizona State University, 132 pp., https://repository.asu.edu/attachments/211431/content/Knutson_asu_0010E_18517.pdf.
- , W. Tang, and P. W. Chan, 2015: Lagrangian coherent structure analysis of terminal winds: Three-dimensionality, intra-model variations, and flight analyses. *Adv. Meteor.*, **2015**, 816727, <https://doi.org/10.1155/2015/816727>.
- Lee, Y. F., and P. W. Chan, 2014: Lidar-based F-factor for wind shear alerting: Different smoothing algorithms and application to departing flights. *Meteor. Appl.*, **21**, 86–93, <https://doi.org/10.1002/met.1434>.
- Miyoshi, T., E. Kalnay, and H. Li, 2013: Estimating and including observation-error correlations in data assimilation. *Inverse Probl. Sci. Eng.*, **21**, 387–398, <https://doi.org/10.1080/17415977.2012.712527>.
- Oude Nijhuis, A. C. P., and Coauthors, 2018: Wind hazard and turbulence monitoring at airports with lidar, radar, and mode-S downlinks: The UFO project. *Bull. Amer. Meteor. Soc.*, **99**, 2275–2293, <https://doi.org/10.1175/BAMS-D-15-00295.1>.
- Pielke, R. A., and Coauthors, 1992: A comprehensive meteorological modeling system—RAMS. *Meteor. Atmos. Phys.*, **49**, 69–91, <https://doi.org/10.1007/BF01025401>.
- Routray, A., U. C. Mohanty, S. R. H. Rizvi, D. Niyogi, K. K. Osuri, and D. Pradhan, 2010: Impact of Doppler weather radar data on numerical forecast of Indian monsoon depressions. *Quart. J. Roy. Meteor. Soc.*, **136**, 1836–1850, <https://doi.org/10.1002/qj.678>.

- Sawada, M., T. Sakai, T. Iwasaki, H. Seko, K. Saito, and T. Miyoshi, 2015: Assimilating high-resolution winds from a Doppler lidar using an ensemble Kalman filter with lateral boundary adjustment. *Tellus*, **67A**, 23473, <https://doi.org/10.3402/TELLUSA.v67.23473>.
- Shun, C. M., and S. Y. Lau, 2002: Implementation of a Doppler light detection and ranging (lidar) system for the Hong Kong International Airport. *10th Conf. on Aviation, Range and Aerospace Meteorology*, Portland, OR, Amer. Meteor. Soc., 8.3, <https://ams.confex.com/ams/pdfpapers/39018.pdf>.
- , and P. W. Chan, 2008: Applications of an infrared Doppler lidar in detection of wind shear. *J. Atmos. Oceanic Technol.*, **25**, 637–655, <https://doi.org/10.1175/2007JTECHA1057.1>.
- Skamarock, W. C., and J. B. Klemp, 2008: A time-split non-hydrostatic atmospheric model for weather research and forecasting applications. *J. Comput. Phys.*, **227**, 3465–3485, <https://doi.org/10.1016/j.jcp.2007.01.037>.
- , and Coauthors, 2019: A description of the Advanced Research WRF Model version 4. NCAR Tech. Note NCAR/TN-556+STR, 145 pp., <https://doi.org/10.5065/1dfh-6p97>.
- Sun, J., and H. Wang, 2013: WRF-ARW variational storm-scale data assimilation: Current capabilities and future developments. *Adv. Meteor.*, **2013**, 815910, <https://doi.org/10.1155/2013/815910>.
- Tang, W., P. W. Chan, and G. Haller, 2010: Accurate extraction of Lagrangian coherent structures over finite domains with application to flight data analysis over Hong Kong International Airport. *Chaos*, **20**, 017502, <https://doi.org/10.1063/1.3276061>.
- , —, and —, 2011a: Lagrangian coherent structure analysis of terminal winds detected by lidar. Part II: Structure evolution and comparison with flight data. *J. Appl. Meteor. Climatol.*, **50**, 2167–2183, <https://doi.org/10.1175/2011JAMC2689.1>.
- , —, and —, 2011b: Lagrangian coherent structure analysis of terminal winds detected by lidar. Part I: Turbulence structures. *J. Appl. Meteor. Climatol.*, **50**, 325–338, <https://doi.org/10.1175/2010JAMC2508.1>.
- Wang, H., J. Sun, X. Zhang, X.-Y. Huang, and T. Auligne, 2013: Radar data assimilation with WRF 4D-VAR. Part I: System development and preliminary testing. *Mon. Wea. Rev.*, **141**, 2224–2244, <https://doi.org/10.1175/MWR-D-12-00168.1>.
- Wong, W. K., and P. W. Chan, 2013: *Data Assimilation of Weather Radar and Lidar for Convection Forecasting and Windshear Alerting in Aviation Applications*. Vol. II, *Data Assimilation for Atmospheric, Oceanic and Hydrologic Applications*, S. K. Park and L. Xu, Eds., Springer, 527–554.
- Xiao, Q., and J. Sun, 2007: Multiple-radar data assimilation and short-range quantitative precipitation forecasting of a squall line observed during IHOP_2002. *Mon. Wea. Rev.*, **135**, 3381–3404, <https://doi.org/10.1175/MWR3471.1>.
- , Y.-H. Kuo, J. Sun, W.-C. Lee, E. Lim, Y.-R. Guo, and D. M. Barker, 2005: Assimilation of Doppler radar observations with a regional 3DVAR system: Impact of Doppler velocities on forecasts of a heavy rainfall case. *J. Appl. Meteor.*, **44**, 768–788, <https://doi.org/10.1175/JAM2248.1>.